Heliyon 10 (2024) e37162

Contents lists available at ScienceDirect

Heliyon

journal homepage: www.cell.com/heliyon

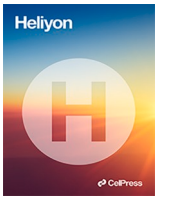

Research article

Numerical investigation of MHD mixed convection in an octagonal heat exchanger containing hybrid nanofluid

Md. Yousuf Ali [a,*], Saiful Islam [b], M.A. Alim [a], Rejowan Ahmed Biplob [c], Md. Zohurul Islam [d]

[a] Department of Mathematics, Bangladesh University of Engineering and Technology, Dhaka, 1000, Bangladesh
[b] Department of Mathematics, Bangabandhu Sheikh Mujibur Rahman Science and Technology University, Gopalganj, 8100, Bangladesh
[c] Department of Electrical and Electronic Engineering, Gono Bishwabidyalay, Dhaka, 1344, Bangladesh
[d] Department of Mathematics, Jashore University of Science and Technology, Jashore, 7408, Bangladesh

ARTICLE INFO

Keywords:
Heat exchanger
Mixed convection
MHD
Response surface
Hybrid nanofluid

ABSTRACT

Nowadays, the advancement of heat transmission for the heat exchanger device is an important field of research for many researchers. In this work, a numerical study has been conducted to investigate the thermal performance of a mixed convective flow through the octagonal heat exchanger covered by hybrid nanofluid (Cu-TiO_2-H_2O). A magnetic field has been introduced inside the cavity to investigate the mixed convective hydrodynamics heat flow characteristics. The nanofluid cores absorb/release energy to manage heat transmission by increasing or decreasing inside the cavity domain as the host fluid and dispersed hybrid nanofluid circulate within the cavity. After transforming the governing equations into a generalized, non-dimensional formulation, the finite element approach is utilized to solve the associated equations. Additionally, response surface methodology is also applied to test the responses of the associated factors. Heat transport was examined in relation to the effects of nanofluids fusion temperature, boundary wall properties, Reynolds number, Hartmann number and nanoparticle volume fractions. The outcomes of this study are analysed by measuring streamline profiles, isotherms, average Nusselt number, velocity profile, and 2D and 3D response surfaces of the computational domain. The underlying flow controlling parameters for instance Reynolds number ($10 \leq Re \leq 200$), Hartmann number ($0 \leq Ha \leq 100$), and nanoparticle volume fractions ($0 \leq \phi \leq 0.1$), the influences have been considered. The findings also reveal that the thermal performance is being boosted due to augmentation of Re and ϕ, but reverse behavior is noticed for *Ha*. Furthermore, the response surfaces obtained from response surfaces methodology express that the Re and ϕ have shown positive influence, and *Ha* has shown negative influence on Nu_{av}. Utilizing a hybrid nanofluid of Cu-TiO_2-H_2O increases the heat transfer capacity of water to 25.75 %. Moreover, the findings could guide to design of a mixed convective heat exchanger for industrial purposes.

1. Introduction

The general composition of hybrid nanofluids is a base fluid (such as ethylene glycol, water, or oil) combined with metallic or non-metallic nanoparticles (Cu, Al_2O_3, Co, Zn, Ag, TiO_2, Fe_3O_4, and so on) to develop the fluid thermal characteristics. The relevance of

* Corresponding author.
E-mail address: yousufmath33@gmail.com (Md.Y. Ali).

https://doi.org/10.1016/j.heliyon.2024.e37162
Received 30 April 2024; Received in revised form 2 August 2024; Accepted 28 August 2024
Available online 30 August 2024

mixed convection in the realm of heat and mass transfer, together with its numerous uses in science and engineering, has drawn a lot of attention to hybrid nanofluid-filled lid-driven cavities in recent years. To improve heat transmission, recently nanoparticles are involved with base fluid to make a hybrid nanofluid. This can lead to a better thermal performance in mixed convection circumstances which is particularly crucial in real-life applications like electronic cooling systems, heat exchangers, computer processors, cooling of nuclear reactors, solar water heating, solar collectors, cooling of electronic tools, and microelectronics [1–4]. In this sense, Maxwell [5] combined micro or millimeter-sized nanoparticles in convectional fluids to create a new kind of heat transmission fluid. Subsequently, Choi et al. [6] combined nanoscale particles with conventional fluids to create an innovative heat transfer fluid known as nanofluids at the National Argonne Laboratory. Additionally, the better qualities of nanofluids such as their reduced sedimentation and clogging force, improved thermal conductivity can improve the heat transfer efficiency of engineering equipment [7–9].

Moreover, magnetohydrodynamic (MHD) has attracted a lot of curiosity from scientists and engineers because of its vast variety of applicability in geophysical research and engineering, including microelectronic packages, solar technologies, cooling nuclear reactors, and reservoirs of geothermal energy. A complicated interplay between the buoyancy effect, which force occurs in the context of natural, mixed convections related to magnetic field impact, which influences fluid flow and heat transfer processes. Islam et al. [10] studied heat transfer enactment including sensitivity analysis of a mixed convective heat exchanger with MHD in a hexagonal cavity utilizing TiO_2-H_2O nanofluid. They observed that including TiO_2 nanoparticles into water expands heat transfer capability of water up to 17.69 %. A 3D numerical simulation was scrutinized by Hakan et al. [11] to investigate the efficiency of heat transmission employing hybrid nanofluids in a newly built thermal system. In another work, Minea et al. [12] used hybrid nanoparticles to study the parabolic solar system, which shows that at 2 % volume levels, the Cu-MgO nanofluid exhibits a noteworthy spike in average Nusselt number (Nu_{av}) with a rise of 14 % as compared to the normal fluid. Kumar et al. [13] investigated the use of a hybrid nanofluid of a T-shaped cavity for double-diffusive flow in a porous medium. Furthermore, some researches using hybrid nanofluid has been done recently to control the mechanics of heat transfer across multiple types of networking devices [14–20].

Additionally, the current generation of researchers is also fascinated with heat transfer and mixed convection fluid motion in closed cavities, where mixed convection is defined as the combination of natural and forced convection. It has recently drawn a lot of interest in the engineering domains due to the ground-breaking applicability of such concerns as heat exchangers, solar panel collectors, and computer cooling mechanisms [21–23]. In actuality, buoyancy forces within an enclosed space and temperature differential have caused natural convection to occur spontaneously. On the other hand, force convection happens when pressure or force exerts from the outside and enters into the cavity. In other words, these two forms of convection happen together for mixed convective analysis. The mixed convective techniques are influenced by the shape and direction of the cavity. In a cavity, mixed convection usually occurs when

Table 1
Previous investigations on mixed convection related to present study.

Investigators	Applied method	Type of fluids	Parameters and ranges	Correlation	Applications	Geometry
Saiful Islam et al. [2]	FEM	Cu-H_2O nanofluid	10^3<Ra<10^6, 0≤Ha≤30, Pr = 6.83	$Nu_{av} = -\frac{K_{nf}}{K_{bf}}\int_S \frac{\partial\theta}{\partial N}dS$	a, b, c, d, e, f, p	prismatic heat exchanger
Abdel-Nour et al. [21]	FEM	Cu-Al_2O_3 hybrid nanofluid	0≤Ha≤100, 10^3≤Ra≤10^6, 10^{-5}≤Da≤10^{-2}	$Nu_{av} = \frac{1}{L}\int_0^L Nu_{local}dL$	b, e, g, i, k, n, s, t, u	porous square cavity
Rowsanara et al. [30]	FEM	Ag-Al_2O_3 hybrid nanofluid	0≤Ha≤50, 0.01≤Ri ≤ 10	$Nu_{av} = \frac{1}{L_h}\int_{L/3}^{2L/3} -\frac{k_{hbnf}}{k_f}\frac{\partial\theta}{\partial X}dY$	a, c, h, j, m, p, s, u, w	multiple rotating cylinder
Mandal et al. [31]	TDMA	H_2O-Cu-Al_2O_3 hybrid nanofluid	10 ≤ Re ≤ 300, 0 ≤ Ha ≤70, 0 ≤ ϕ ≤ 0.02, 0.1 ≤ Ri ≤ 100	$Nu = \frac{k}{k_f}\frac{1}{S}\int_0^S\left(-\frac{\partial\theta}{\partial N}\Big\vert_{\text{wavy wall}}\right)dS$	a, g, h, m, q, s, t, x, y	porous wavy cavity
Saha et al. [32]	FEM	H_2O-Al_2O_3 nanofluid	10^4<Ra<10^6, 0≤Ha≤50, 0≤ ϕ ≤ 0.05	$Nu_{av} = \left(\frac{k_{nf}}{k_{bf}}\right)\int\frac{\partial\theta}{\partial Y}dX$	d, n, o, r, u, w	square wavy cavity
Zeghbid et al. [33]	FVM	Cu, Ag, Al_2O_3, TiO_2-H_2O	0.1≤ Ri ≤ 100, 0≤ ϕ ≤ 1, 10^3≤Ra≤10^5	$S_t = \int S_{gen}dV$	a, c g, j, k, r, t, u, w	square lid driven cavity
Maneengam et al. [34]	GFEM	Fe_3O_4-MWCNT-H_2O	0 ≤ Ha ≤100 − 500, ≤ Ω ≤ 1000, 10^{-2} ≤ Da ≤10^{-5}	$Nu_{ave} = \frac{1}{S^2}\int_0^S\int_0^S Nu_{loc}\,dy\,dz$	b, h, k, m,o, p, r, u, v, y	3D porous cavity
Alipour et al. [35]	GFEM, CVFEM	H_2O- Al_2O_3-ethylene glycol	100≤Ra≤1500, 0≤Ha≤40	$Nu_{ave} = \frac{1}{2\pi}\int_0^{2\pi} Nu_{loc}\,dr$	c, d, m, o, p, r, v, w	trapezoidal porous cavity

*FEM= Finite element method, FVM= Finite volume method, TDMA = Tri-diagonal matrix algorithm, HGF= Higher geometric function, GFEM = Galerkin finite element method.

**(a) heat exchangers; (b) home ventilation; (c) solar collectors; (d) cooling organisms in nuclear reactors; (e) petroleum reservoirs; (f) fire engineering; (g) blood flow control; (h) food processing; (i) paints manufacturing; (j) cancer and tumor treatment; (k) glass fiber manufacturing; (l) shampoo manufacturing; (m) nuclear power plant; (n) solar energy; ((o) cooling of electronic device; (p) cooling of nuclear reactors; (q) geothermal reservoirs; (r) material built-up machinery; (s) gas industries; (t) polymer industries; (u) refrigerator; (v) chemical industry; (w) home ventilation.

there is generated ventilation or a lid velocity on any walls of structure. Scholars conducted a range of investigations on mixed convection using nanofluid. For instance, Yeasmin et al. [24] explored mixed convective heat transfer in a porous lid-driven L-shaped cavity, and concluded that to improve convective heat transfer rate, a greater Darcy number is suggested for inflow conditions. In the context of two spinning cylinders, Garmroodi et al. [25] completed a computational study for MHD and mixed convection in a lid-driven cavity containing a Cu-water nanofluid. The authors demonstrated that mixed convection increases with the circular motion of two circuits, and the intensity of heat transfer falls as Hartmann number (*Ha*) increases using the multi-phase mixer model and the finite volume technique. Afterward, Ishak et al. [26] explored mixed convection with entropy production in a closed cavity containing a solid cylinder and nanofluid using finite element method (FEM). They declared that the location of solid body and size had a substantial effect on heat transfer and Bejan number within the chamber. In a double-wall lid-driven enclosure with a heat transmission barrier and an electrical field, Ali et al. [27] examined mixed convective Casson fluid motion and identified a large proportion of temperature transfer increase for the proper direction of lid wall. They found that with increasing Casson fluid parameter and Reynolds number, the heat transfer capability boosted up. Later, Ali et al. [28] also conducted another analysis on flow and thermal characteristics in a hollow controlled by a lid and included a revolving flat plate that was exposed to a magnetic field. Their findings guaranteed a 123.03 % improvement in heat transmission while employing 5 % Al_2O_3 nanoparticles into the nanofluid mixer.

Researchers enhanced hybrid nanofluids, made up of several nanoparticles into a base fluid, for increasing the heat transfer performance much better. The mixture of component nanoparticles in traditional base fluids is connected with the efficacy of hybrid nanofluids. Furthermore, in contrast to mono-nanofluids, hybrid nanofluids also offer more stable, chemically inert, and affordable characteristics. A study about entropy generation for mixed convection in a horizontal channel with a square obstruction containing hybrid nanofluids was completed by Hussain et al. [29]. They anticipated that while magnetic entropy production increases, fluid velocity and heat transport production decrease due to rising magnetic field intensity. In a partially heated square cavity, Akhter et al. [30] applied FEM to investigate mixed convection utilizing hybrid nanofluid that contains also a magnetic field and a spinning cylinder. Mandal et al. [31] used Cu and Al_2O_3 nanoparticle into water to examine the hydrothermal characteristics of nanofluids in a porous complex enclosure with a uniform magnetic field, where hybrid nanofluids provide a developed heat transfer performance rather than other mono-nanofluids. Table 1 summarizes the literature of prior statistical efforts that depict mixed convection into various confinement types and is relevant to the current investigation.

As per the previously mentioned literature, it is evident that researchers are highly intrigued by MHD mixed convective heat exchangers because of its innovative application in a wide range of engineering domains, particularly in the design of numerous industrial architects with different geometrical structure. A few research on octagonal enclosures containing different nanoparticles has been conducted recently [36,37], even though separate investigations on diverse closed cavities with varying MHD mixed convection were performed at different stages. The study on the formulation of such heat exchanger devices that can transfer heat energy quickly is very limited [38–40]. The proposed novel heat exchanger device can transfer heat energy between two or more fluids. The prime aim of this underlying model is to illustrate the consequence of employing hybrid nanofluid in a mixed convective octagonal heat exchanger filled with Cu-TiO_2-H_2O nanofluid, where an exterior uniform magnetic field is present. In order to analyze the enhancement of energy shifting efficiency by the proposed system, we furthermore conducted a statistical technique called response surface methodology (RSM). In this method, the combined impact of significant factors on the rate of heat transfer calculation was assessed for different flow controlling parameters to get the optimal heat transfer. Different 2D and 3D response surfaces are explained physical explanation by the use of RSM. Although multiple numerical studies on octagonal cavities containing nanofluid have been conducted at various times, we use hybrid nanoparticles with MHD in this study, which is one of the novelty of the present study. Furthermore, to the best of the author's knowledge, the analysis of heat transfer behavior using FEM and RSM is the most new aspect of this work. This study uses numerical and statistical approaches to analyze the Reynolds number (Re), Hartmann number (*Ha*), and nanoparticle volume fraction (ϕ) in a mixed convective octagonal heat exchanger.

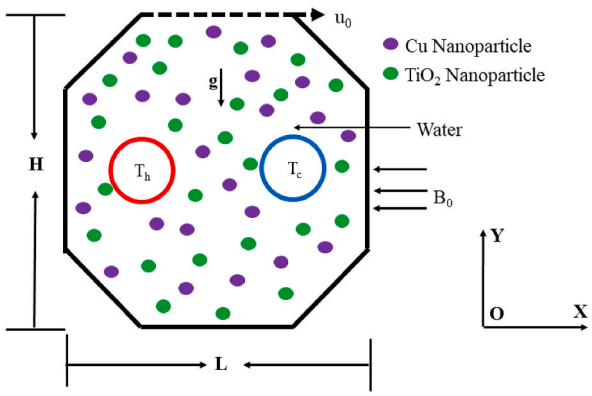

Fig. 1. Physical model of proposed octagonal heat exchanger.

2. Mathematical framework

2.1. Physical description

An octagonal-shaped heat exchanger is considered as a fluid domain covered by Titanium oxide (TiO_2) and Copper (Cu) solid nanoparticles, and H_2O as a common fluid. This mixture is taken 2D steady Newtonian incompressible flow with an external magnetic field. The heat exchanger's length and height are L and H respectively, with two cylindrical pipes (radius 0.1 L) serving as a heater on the left and a cooler on the right side of the domain. The upper straight wall is traveling a lid velocity u_0. The physical alignment of this model using hybrid nanofluid is shown in Fig. 1. Here, the right cylindrical pipe taken to be a cooled surface (T_c), while the left pipe considered as a heated surface (T_h). The external shielded barriers of the fluid realm are entirely insulated. Moreover, the gravitational force (g) acts in the opposite track of the Y-axis. Additionally, a continuous magnetic field B_0 around the container runs from the right to the left. Furthermore, the neighboring media being considered no slip, and TiO_2 and Cu nanoparticles are uniform in shape. The thermophysical appearances of the considered nanoparticles and base fluid are shown in Table 2. The fluid flow region is seen and completed using a 2D Cartesian layout, where the left wall is indicated by the Y-direction and the bottom wall is shown by the X-direction.

2.2. Governing equations

To make a proper mathematical model for this proposed hybrid nanofluid model, the following well-known continuity, momentum, and energy equations are formed with MHD interference [29,32]:

$$\frac{\partial u}{\partial x}+\frac{\partial v}{\partial y}=0 \tag{1}$$

$$\rho_{hnf}\left(u\frac{\partial u}{\partial x}+v\frac{\partial u}{\partial y}\right)=-\frac{\partial p}{\partial x}+\mu_{hnf}\left(\nabla^2 u\right) \tag{2a}$$

$$\rho_{hnf}\left(u\frac{\partial v}{\partial x}+v\frac{\partial v}{\partial y}\right)=-\frac{\partial p}{\partial y}+\mu_{hnf}\left(\nabla^2 v\right)+g(\rho\beta)_{hnf}(T-T_c)-\sigma_{hnf}B_0^2 v \tag{2b}$$

$$\left(\rho c_p\right)_{hnf}\left(u\frac{\partial T}{\partial x}+v\frac{\partial T}{\partial y}\right)=\kappa_{hnf}\left(\frac{\partial^2 T}{\partial x^2}+\frac{\partial^2 T}{\partial y^2}\right) \tag{3}$$

There are some essential initial and boundary conditions of the proposed heat exchanger model:

$$\left.\begin{array}{l}\text{at left circular edge}, u=0, v=0, T=T_h\\ \text{at right circular edge}, u=0, v=0, T=T_c\\ \text{at top horizontal wall}, u=u_0, v=0, \dfrac{\partial T}{\partial y}=0\\ \text{and all surrounding walls}, u=v=0, \dfrac{\partial T}{\partial n}=0\end{array}\right\} \tag{4}$$

where, the vector acting perpendicularly on the heated surface is denoted by n.

2.3. Correlations of hybrid nanofluid

The thermo-physical characteristics of base fluid (H_2O) and nanomaterials (Cu and TiO_2) are discussed in the current subsection. In actuality, the features of the base fluid and nanomaterials determine the features of the nanofluid. Thus, the regression coefficients in Table 3 are used to compute the appearances of the hybrid nanofluid.

2.4. Dimensional analysis

To transform the governing equations (1)–(3) into dimensionless form, we define the subsequent non-dimensional variables along with the boundary conditions (4):

Table 2
Thermophysical properties of the solid particle and base fluid [31,41].

Base fluid & nanoparticles	ρ	c_p	κ	σ	β	μ	Pr
H_2O	997.1	4179	0.613	5.5×10^{-6}	2.1×10^{-4}	8.91×10^{-4}	6.9
Cu	8933	385	401	5.96×10^{7}	1.67×10^{-5}	–	–
TiO_2	4250	686.2	8.953	3.5×10^{6}	0.9×10^{-5}	–	–

Table 3
Correlations of hybrid nanofluid between nanoparticles and base fluid.

Properties of Hybrid Nanofluid's		Applied correlations
Concentration of nanoparticles:	:	$\phi = \phi_{Cu} + \phi_{TiO_2}$
Density of nanofluid:	:	$\rho_{hnf} = (1-\phi)\,\rho_{bf} + \phi\,\rho_{sp}$ where $\phi\rho_{sp} = \phi_{Cu}\rho_{Cu} + \phi_{TiO_2}\rho_{TiO_2}$
Specific heat capacity:	:	$(\rho c_p)_{hnf} = (1-\phi)(\rho c_p)_{bf} + \phi(\rho c_p)_{sp}$ where $\phi(\rho c_p)_{sp} = \phi_{Cu}(\rho c_p)_{Cu} + \phi_{TiO_2}(\rho c_p)_{TiO_2}$
Thermal conductivity	:	$k_{hnf} = k_{bf}\left\{\frac{k_{sp} + 2k_{bf} - 2\phi(k_{bf} - k_{sp})}{k_{sp} + 2k_{bf} + \phi(k_{bf} - k_{sp})}\right\}$ where $\phi k_{sp} = \phi_{Cu}k_{Cu} + \phi_{TiO_2}k_{TiO_2}$
Thermal diffusivity	:	$\alpha_{hnf} = \frac{\kappa_{hnf}}{(\rho c_p)_{hnf}}$
Dynamic viscosity	:	$\mu_{hnf} = \mu_{bf}(1 + 2.5\phi + 6.5\phi^2)$
Thermal expansion coefficient	:	$(\rho\beta)_{hnf} = (1-\phi)(\rho\beta)_{bf} + \phi(\rho\beta)_{sp}$ where $\phi(\rho\beta)_{sp} = \phi_{Cu}(\rho\beta)_{Cu} + \phi_{TiO_2}(\rho\beta)_{TiO_2}$
Electrical conductivity	:	$\sigma_{hnf} = \sigma_{bf}\left[1 + \frac{3\phi\left(\frac{\sigma_{sp}}{\sigma_{bf}} - 1\right)}{\left(\frac{\sigma_{sp}}{\sigma_{bf}} + 2\right) - \phi\left(\frac{\sigma_{sp}}{\sigma_{bf}} - 1\right)}\right]$ where $\phi\sigma_{sp} = \phi_{Cu}\sigma_{Cu} + \phi_{TiO_2}\sigma_{TiO_2}$

$$X = \frac{x}{L}, Y = \frac{y}{L}, U = \frac{u}{u_0}, V = \frac{v}{u_0}, P = \frac{p}{\rho_{bf}\,u_0^2} \text{ and } \theta = \frac{T - T_c}{T_h - T_c}$$

The following is a presentation of the non-dimensional versions of the involved dimensional governing equations:

$$\frac{\partial U}{\partial X} + \frac{\partial V}{\partial Y} = 0 \tag{5}$$

$$U\frac{\partial U}{\partial X} + V\frac{\partial U}{\partial Y} = -\left(\frac{\rho_{bf}}{\rho_{hnf}}\right)\frac{\partial P}{\partial X} + \left(\frac{\mu_{hnf}}{\mu_{bf}}.\frac{\rho_{bf}}{\rho_{hnf}}\right)\Pr\left(\nabla^2 U\right) \tag{6}$$

$$U\frac{\partial V}{\partial X} + V\frac{\partial V}{\partial Y} = -\left(\frac{\rho_{bf}}{\rho_{hnf}}\right)\frac{\partial P}{\partial Y} + \left(\frac{\mu_{hnf}}{\mu_{bf}}.\frac{\rho_{bf}}{\rho_{hnf}}\right)\Pr\left(\nabla^2 V\right) + \frac{(\rho\beta)_{hnf}}{\rho_{hnf}\beta_{bf}}Ri\theta - \left(\frac{\rho_{bf}}{\rho_{hnf}}.\frac{\sigma_{hnf}}{\sigma_{bf}}\right)\frac{1}{Re}Ha^2\,V \tag{7}$$

$$U\frac{\partial \theta}{\partial X} + V\frac{\partial \theta}{\partial Y} = \left(\frac{\alpha_{hnf}}{\alpha_{bf}}\right)\nabla^2\theta \tag{8}$$

Here, Richardson number (Ri), Prandtl number (Pr) and Hartmann number (*Ha*) are three significant parameter generated form above equation, respectively as: $Ri = \frac{g\,\beta_{bf}(T_h - T_c)}{v_0}$, $Pr = \frac{v_{bf}}{\alpha_{bf}}$ and $Ha = B_0 L\sqrt{\frac{\sigma_{bf}}{\mu_{bf}}}$. Moreover, the dimension free boundary conditions reformed as:

$$\left.\begin{array}{c} \text{on left circular edge}, U = V = 0, \theta = 1 \\ \text{on right circular edge}, U = V = 0, \theta = 0 \\ \text{on the top horizontal wall}, U = U_0, V = 0, \frac{\partial\theta}{\partial Y} = 0 \\ \text{and on all surrounding walls}, U = V = 0, \frac{\partial\theta}{\partial N} = 0 \end{array}\right\} \tag{9}$$

Additionally, from the heated wall, the average Nusselt number (Nu_{av}) is ascertained by:

$$Nu_{av} = -\left(\frac{k_{hnf}}{k_{bf}}\right)\int_{HS}\frac{\partial\theta}{\partial N}\,dS \tag{10}$$

Moreover, the stream function ψ is defined as: $U = \frac{\partial\psi}{\partial Y}, V = -\frac{\partial\psi}{\partial X}$. In this case, the positive sign denotes the streamlines' anticlockwise circulation, while the negative sign denotes their clockwise circulation. Therefore, $\frac{\partial^2\psi}{\partial X^2} + \frac{\partial^2\psi}{\partial Y^2} = -\left(\frac{\partial V}{\partial X} - \frac{\partial U}{\partial Y}\right) = -\Omega$ is the equation of vorticity, and the vorticity vector is Ω.

3. Numerical analysis

3.1. Computational technique

The associated equations are expressed in dimensionless form to avoid dimensional dependencies. Equations (5)–(8) related to initial and boundary conditions (9) are computed numerically applying the Galerkin finite element method. To get the finite element

equations, the weighted residuals approach, as previously reported by Sienkiewicz and Taylor [36], is applied in equations (5)–(8) as:

$$\int_A N_\alpha \left(\frac{\partial U}{\partial X}+\frac{\partial V}{\partial Y}\right) dA = 0 \tag{11}$$

$$\int_A N_\alpha \left(U\frac{\partial U}{\partial X}+V\frac{\partial U}{\partial Y}\right) dA = -\left(\frac{\rho_{bf}}{\rho_{hnf}}\right)\int_A H_\lambda \left(\frac{\partial P}{\partial X}\right) dA + \left(\frac{\mu_{hnf}}{\mu_{bf}}.\frac{\rho_{bf}}{\rho_{hnf}}\right)\ \frac{1}{Re}\int_A N_a \left(\frac{\partial^2 U}{\partial X^2}+\frac{\partial^2 U}{\partial Y^2}\right) dA \tag{12}$$

$$\begin{aligned}\int_A N_\alpha \left(U\frac{\partial V}{\partial X}+V\frac{\partial V}{\partial Y}\right) dA = &-\frac{\rho_{bf}}{\rho_{hnf}}\int_A H_\lambda \left(\frac{\partial P}{\partial Y}\right) dA + \left(\frac{\mu_{hnf}}{\mu_{bf}}.\frac{\rho_{bf}}{\rho_{hnf}}\right)\ \frac{1}{Re}\int_A N_a \left(\frac{\partial^2 V}{\partial X^2}+\frac{\partial^2 V}{\partial Y^2}\right) dA \\ &+\left\{\frac{(\rho\beta)_{hnf}}{\rho_{hnf}\beta_{bf}}\right\} Ri\int_A N_\alpha \theta dA - \left(\frac{\rho_{bf}}{\rho_{hnf}}.\frac{\sigma_{hnf}}{\sigma_{bf}}\right)\ \frac{Ha^2 V}{Re}\int_A N_\alpha V dA\Bigg\}\end{aligned} \tag{13}$$

$$\int_A N_\alpha \left(U\frac{\partial \theta}{\partial X}+V\frac{\partial \theta}{\partial Y}\right) dA = \left(\frac{\alpha_{hnf}}{\alpha_{bf}}\right)\ \frac{1}{RePr}\int_A N_A \left(\frac{\partial^2 \theta}{\partial X^2}+\frac{\partial^2 \theta}{\partial Y^2}\right) dA \tag{14}$$

Here, N_a (a = 1, 2. … …, 6) represents the element's interpolation functions, A is the area of element, and H_λ (λ = l, 2, 3) denotes the interpolation functions for pressure. After that, in equations (12)–(14), the Gauss's theorem is involved to create the boundary integral terms related to the heat flux and surface tractions. Then equations (12)–(14) converted to:

$$\begin{aligned}\int_A N_\alpha \left(U\frac{\partial U}{\partial X}+V\frac{\partial U}{\partial Y}\right) dA + \int_A H_\lambda \left(\frac{\partial P}{\partial Y}\right) dA + \left(\frac{\mu_{hnf}}{\rho_{nf}\nu_{nf}}\right)\ \frac{1}{Re}\int_A \left(\frac{\partial N_\alpha}{\partial X}\frac{\partial U}{\partial X}+\frac{\partial N_\alpha}{\partial Y}\frac{\partial U}{\partial Y}\right) dA \\ = \int_{S_0} N_\alpha S_x dS_0\Bigg\}\end{aligned} \tag{15}$$

$$\begin{aligned}&\int_A N_\alpha \left(U\frac{\partial V}{\partial X}+V\frac{\partial V}{\partial Y}\right) dA + \int_A H_\lambda \left(\frac{\partial P}{\partial Y}\right) dA + \left(\frac{\mu_{hnf}}{\rho_{hnf}\nu_{bf}}\right)\ \frac{1}{Re}\int_A \left(\frac{\partial N_\alpha}{\partial X}\frac{\partial V}{\partial X}+\frac{\partial N_\alpha}{\partial Y}\frac{\partial V}{\partial Y}\right) dA \\ &-\left\{\frac{(\rho\beta_{hnf})}{\rho_{hnf}\beta_{bf}}\right\} Ri\int_A N_\alpha \theta dA + \left(\frac{\rho_{bf}}{\rho_{hnf}}.\frac{\sigma_{hnf}}{\sigma_{bf}}\right)\ \frac{Ha^2}{Re}\int_A N_\alpha V dA = \int_{S_0} N_\alpha S_y dS_0\Bigg\}\end{aligned} \tag{16}$$

$$\int_A N_\alpha \left(U\frac{\partial \theta}{\partial X}+V\frac{\partial \theta}{\partial Y}\right) dA + \left(\frac{\alpha_{hnf}}{\alpha_{bf}}\right)\ \frac{1}{RePr}\int_A \left(\frac{\partial N_\alpha}{\partial X}\frac{\partial \theta}{\partial X}+\frac{\partial N_\alpha}{\partial Y}\frac{\partial \theta}{\partial Y}\right) dA = \int_{S_W} N_\alpha q_{1w} dS_w \tag{17}$$

Here, S_x and S_y are surface tractions, S_0 is outflow barrier, together with the heat flux (q_w) that flow into or out of the domain along the boundary wall (S_w). The velocity components U, V, temperature θ, and pressure, P are the essential unknowns for the differential equations that come before. The finite element equations in this study are developed using the six-node triangular element. Only the corner nodes are connected to pressure; the other six nodes are only connected to temperature and velocities. Also, consider:

$$U(X,Y) = N_\beta U_\beta, V(X,Y) = N_\beta V_\beta, \theta(X,Y) = N_\beta \theta_\beta, P(X,Y) = H_\lambda P_\lambda \tag{18}$$

where,β = 1,2,……,6,and λ = 1,2,3. Substituting this into (11) and equations 15–17, the finite element equations can be written as:

$$R_{\alpha\beta^x} U_\beta + R_{\alpha\beta^y} V_\beta = 0 \tag{19}$$

$$R_{\alpha\beta\gamma^x} U_\beta U_\gamma + R_{\alpha\beta\gamma^y} V_\beta U_\gamma + M_{\lambda\mu^x} P_\mu + \left(\frac{\mu_{hnf}}{\rho_{hnf}\nu_{bf}}\right)\ \frac{1}{Re}\left(S_{\alpha\beta^{xx}} + S_{\alpha\beta^{yy}}\right) U_\beta = Q_{\alpha^u} \tag{20}$$

$$\begin{aligned}R_{\alpha\beta\gamma^x} U_\beta V_\gamma + R_{\alpha\beta\gamma^y} V_\gamma V_\gamma + M_{\alpha\mu^y} P_\mu + \left(\frac{\mu_{hnf}}{\rho_{hnf}\nu_f}\right)\ \frac{1}{Re}\left(S_{\alpha\beta^{xx}} + S_{\alpha\beta^{yy}}\right) V_\beta - \frac{(\rho\beta)_{hnf}}{\rho_{hnf}\beta_{bf}} Ri R_{\alpha\beta}\theta_\beta \\ + \frac{\rho_{bf}\sigma_{hnf}}{\rho_{hnf}\sigma_{bf}}\frac{Ha^2}{Re} R_{\alpha\beta} V_\beta = Q_{\alpha^v}\Bigg\}\end{aligned} \tag{21}$$

$$R_{\alpha\beta\gamma^x} U_\beta \theta_\gamma + R_{\alpha\beta\gamma^y} V_\beta \theta_\gamma + \frac{\alpha_{hnf}}{\alpha_{bf}}\ \frac{1}{RePr}\left(S_{\alpha\beta^{xx}} + S_{\alpha\beta^{yy}}\right)\theta_\beta = Q_{\alpha^\theta} \tag{22}$$

where the coefficients concluded the element area and edges are as follows:

$$\left.\begin{aligned} R_{\alpha\beta^x} &= \int_A N_\alpha N_{\beta,x} dA;\ R_{\alpha\beta^y} = \int_A N_\alpha N_{\beta,y} dA; R_{\alpha\beta\gamma^x} = \int_A N_\alpha N_\beta N_{\gamma,x} dA; \\ R_{\alpha\beta\gamma^y} &= \int_A N_\alpha N_\beta N_{\gamma,y} dA; R_{\alpha\beta} = \int_A N_\alpha N_\beta dA; S_{\alpha\beta^{xx}} = \int_A N_{\alpha,x} N_{\beta,x} dA; \\ S_{\alpha\beta^{yy}} &= \int_A N_{\alpha,y} N_{\beta,y} dA; M_{\lambda\mu^x} = \int_A H_\lambda H_{\mu,x} dA; M_{\alpha\mu^y} = \int_A H_\alpha H_{\mu,y} dA; \\ Q_{\alpha^u} &= \int_{S_0} N_\alpha S_x dS_0; Q_{\alpha^v} = \int_{S_0} N_\alpha S_y dS_0; Q_{\alpha^\theta} = \int_{S_W} N_\alpha q_w dS_w; \end{aligned}\right\} \tag{23}$$

These element matrices are prepared for numerical simulation after a closed-form analysis. The comprehensive computations process is also existing in Refs. [42,43]. The element nodal velocity, temperatures, and pressure components are thus transformed into a set of algebraic equations, with the progressive unknowns expressed as follows:

$$\begin{bmatrix} R_{uu} & R_{uv} & R_{u\theta} & R_{up} \\ R_{vu} & R_{vv} & R_{v\theta} & R_{vp} \\ R_{\theta u} & R_{\theta v} & R_{\theta\theta} & 0 \\ R_{pu} & R_{pv} & 0 & 0 \end{bmatrix} \begin{bmatrix} \Delta u \\ \Delta v \\ \Delta\theta \\ \Delta p \end{bmatrix} = \begin{bmatrix} F_{\alpha^u} \\ F_{\alpha^v} \\ F_{\alpha^\theta} \\ F_{\alpha^p} \end{bmatrix} \tag{24}$$

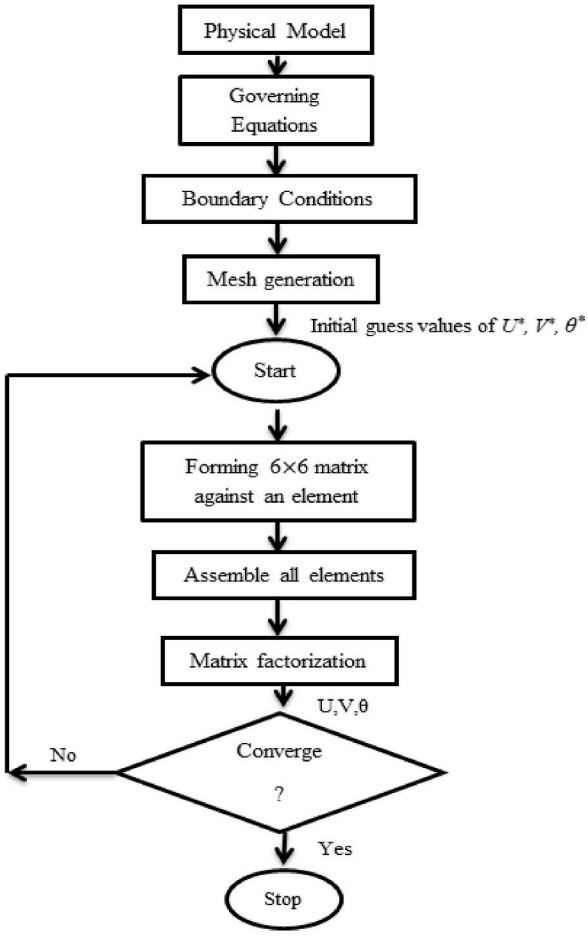

Fig. 2. An extensive flow diagram for the computation method.

$$\left.\begin{aligned}
R_{uu} &= R_{\alpha\beta\gamma^x}U_\beta + R_{\alpha\beta\gamma^x}U_\gamma + R_{\alpha\beta\gamma^y}V_\beta + \left(\frac{\mu_{hnf}}{\rho_{hnf}\nu_{bf}}\right)\frac{1}{Re}\left(S_{\alpha\beta^{xx}} + S_{\alpha\beta^{xy}}\right);\\
R_{uv} &= R_{\alpha\beta\gamma^y}U\gamma; R_{u\theta} = 0; R_{up} = M_{\alpha\mu^x}; R_{vu} = R_{\alpha\beta\gamma^x}V\gamma; R_{vp} = R_{\alpha\mu^y};\\
R_{vv} &= R_{\alpha\beta\gamma^x}U_\beta + R_{\alpha\beta\gamma^y}V_\gamma + \left(\frac{\mu_{hnf}}{\rho_{hnf}\nu_{bf}}\right)\frac{1}{Re}\left(S_{\alpha\beta^{xx}} + S_{\alpha\beta^{xy}}\right);\\
R_{v\theta} &= -\frac{(\rho\beta)_{hnf}}{\rho_{hnf}\beta_{bf}}RiR_{\alpha\beta}; R_{\theta u} = R_{\alpha\beta\gamma^x}\theta\gamma; R_{\theta v} = R_{\alpha\beta\gamma^y}\theta\gamma;\\
R_{\theta\theta} &= R_{\alpha\beta\gamma^x}U_\beta + R_{\alpha\beta\gamma^y}V_\beta + \left(\frac{\alpha_{hnf}}{\alpha_{bf}}\right)\frac{1}{RePr}\left(S_{\alpha\beta^{xx}} + S_{\alpha\beta^{xy}}\right);\\
R_{pu} &= M_{\alpha\mu^x}; R_{pv} = M_{\alpha\mu^y}; \text{ and } R_{\theta p} = R_{p\theta} = R_{pp} = 0;
\end{aligned}\right\} \tag{25}$$

After that, the PDE solver in MATLAB has been used to modify the Newton-Raphson iteration approach for solving these nonlinear algebraic equations. Solutions are considered to have converged when the relative error of each variable across successive iterations is less than the convergence criteria ε, meaning that, $|\psi^{n+1} - \psi^n| < \varepsilon$, where n is a number of iteration and $\psi = \psi(U, V, \theta)$. The convergence criterion is set to $\varepsilon = 10^{-5}$. When comparing FEM to other numerical techniques, there are a number of advantages. One of them is that the equations for each element are determined using FEM. Therefore, it is not a major problem to add new pieces by refining old ones. The approach is helpful for addressing boundary value problems in a range of engineering applications because it uses a set of finite elements to generate computational domains with irregular geometries. A detailed explanation of this method was explained in Ref. [44]. Also, Fig. 2 describes a detailed flowchart of this computational method.

3.2. Grid sensitivity analysis

In order to get suitable number of elements for discretization that may be used for FEM, the grid test with the following parameters is explained: $\phi = 0.02$, $Ha = 50$, $\mathrm{Re} = 100$, and $\mathrm{Pr} = 6.9$. Here, the value of $\mathrm{Nu_{av}}$ is designated in order to apply the sensitivity test for generating the appropriate meshing of the computational domain. This whole computational domain is divided into five dissimilar quantities of triangular-shaped elements (1992, 2890, 6526, 18958, and 23760). A triangular meshing example is shown in Fig. 3. Additionally, the computed values of $\mathrm{Nu_{av}}$ for varied numbers of triangle members in this fluid domain are displayed in Table 4 and Fig. 3. The value of $\mathrm{Nu_{av}}$ for 18958 elements is almost the same as the value determined for the following higher component number. Because of this, it is preferred to mesh and finish this fluid model using the 18958 triangular pieces.

3.3. Code validation

Before initiating the study, the underlying model was verified comprehensively with existing studies conducted by some authors. Firstly, the outcomes (streamlines and isotherms) of Islam et al. [45] is compared, in Fig. 4, to prove the validation of present study. It is clearly visible from Fig. 4 that the pattern of streamlines and isotherm from Islam et al. [45] study and our outcomes are quite similar, which give strong encouragement to validate the present work. The number of two symmetric vortices from Islam et al. [45] study has been produced similar two symmetric vortices, and the patterns of the streamlines has been made the similar trajectories (Fig. 4(a)). It

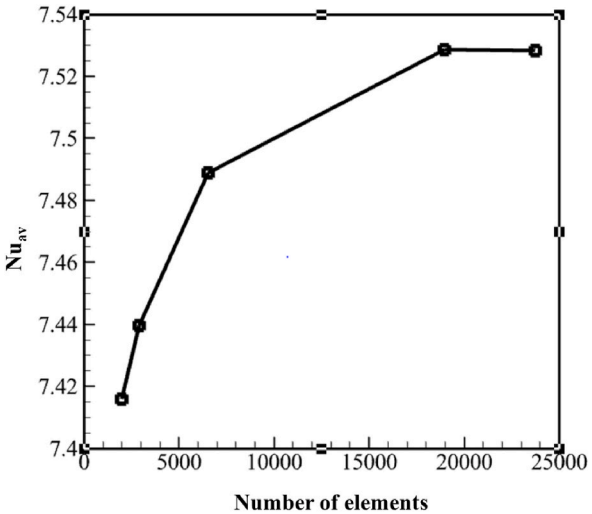

Fig. 3. Grid sensitivity analysis.

Table 4
Grid independence check for current study.

Elements	1992	2890	6526	18958	23760
$\mathbf{Nu_{av}}$	7.4158	7.4395	7.4890	7.5285	7.5283

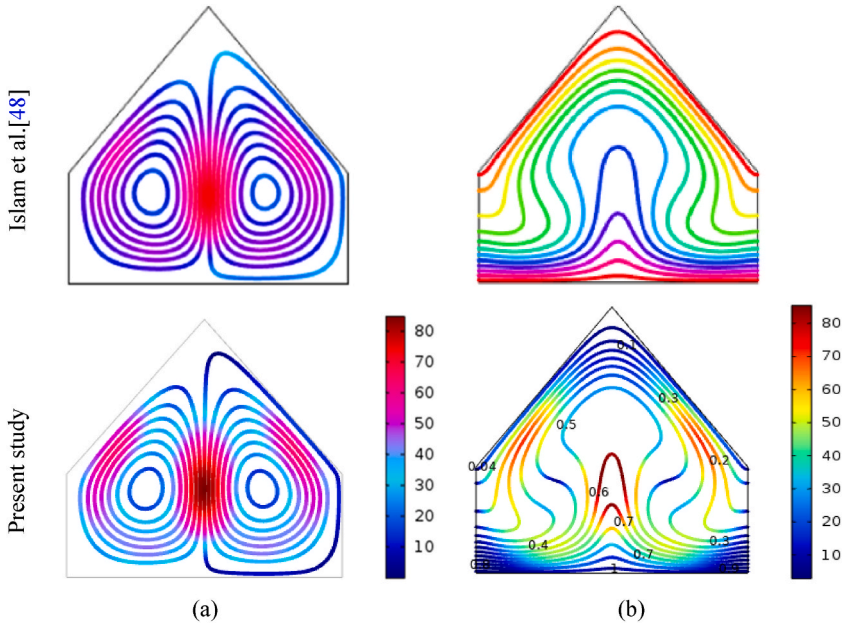

Fig. 4. Compareing (a) streamlines, and (b) isotherms of current study (bottom panels) with Islam et al. [45] (top panels).

is also observed that the heat energy has been produced in the middle of the streamline contour, which clearly supports the findings from proposed model. Looking at the isotherms contour analysis, the isotherm profiles distribution from Islam et al. [45] study and present study are found to be very similar distribution (Fig. 4(b)). The stratification of the isotherms from present study are fully isolated from the Islam et al. [45] study.

In addition to these analyses, we have also formulated another model by inserting two blocks inside the cavity. The code was again validated by optimizing the flow controlling parameters for this model. The hydrodynamic parameters were also taken into account for

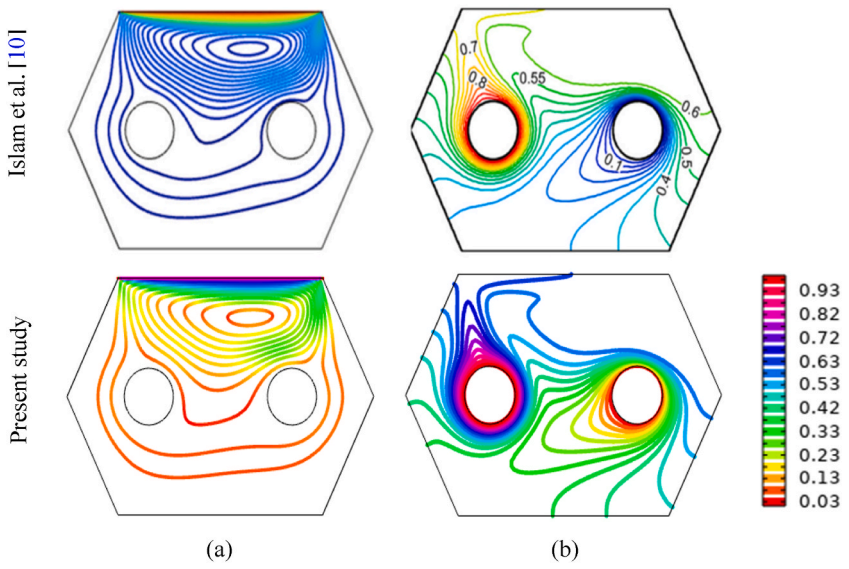

Fig. 5. Compareing (a) streamlines, and (b) isotherms of our result (bottom panels) and Islam et al.'s [10] (top panels).

the model as need as possible by the authors Islam et al. [10]for numerical calculation. The obtained streamlines and isotherms profile were also then compared with the study conducted by Islam et al. [10] investigation. as illustrated in Fig. 5. It is evident that a single vortex has been produced near the top wall of the hexagonal cavity in both of the studies (Islam et al. [10] top and present study bottom) as seen in the streamline analysis (Fig. 5(a)). The obtained isotherm profiles are displayed the thermal stratification from Islam et al. [45] study and the present study. The trajectories of the isotherm curves are showing the similar distribution within the flow domain for the both of the investigation. Overall, the isotherm profiles from Fig. 5(b), our model can correctly reproduce isotherms curves as the isotherm curves obtained by Islam et al. [45] study.

Furthermore, we compared the average Nusselt number calculated from Islam et al. [10] findings and the Nusselt number from this current model to assess the accuracy of the present model by computing the heat transfer enhancement. The mean Nusselt number was observed for different Reynolds number to compare the heat transfer enhancement capacity of the present model to validate the model without affecting the solution. As it is seen from Table 5, the calculated Nusselt number (by keeping $Ha = 50$ and $\phi = 0.5$ fixed) is growing with the increasing of Reynolds number that strongly aligned with study conducted by Islam et al. [10]. There are some minor deviations between the results (in Table 5) derived from the current numerical model and the Islam et al. [10] model. The highest variations were noticed to be 1.06 %, which are in line with the acceptable range of the standard error calculation for computational investigation. In this regard, the proposed model may be considered as an optimal model and be able to replicate the height accurate outcomes.

4. Results and discussion

In this work, the significant parameters have been utilized to explore the impacts of MHD mixed convective hybrid nanofluid flow within an octagon-shaped heat exchanger. After validating the model, we run the final simulation to store the data for different aspect of the analysis. The observed results are explained inside the cavity using streamline, isotherm contours, and Nu_{av} for various values of Re, *Ha*, and ϕ in Figs. 6–15. Here, Cu-TiO_2-H_2O hybrid nanofluid occupies the octagonal-shaped cavity, where all nanoparticles are employed in spherical form. Additionally, by few some 2D and 3D response surfaces are explained using RSM to explore how Re, *Ha*, and ϕ influence the Nu_{av}. The conventional values are taken to complete this simulation, $Re = 100$, $Ha = 10$, $\phi = 0.02$, $Ri = 1$, and $Pr = 6.9$.

4.1. Impact of Reynolds number

For this mixed convective framework, the streamline, isotherm contours, and Nusselt number in Figs. 6–7 reveal the influence of Re. Fig. 6(a) illustrates the way to regulate $Re = (10–200)$ on the fluid's flow pattern through streamline contours assuming $Pr = 6.9$, $Ri = 1$, $Ha = 10$, and $\phi = 0.02$. The fluid motion is increased by higher values of Re, which ultimately causes a noticeable enhancement in streamline distribution and flow rotation magnitude. Due to the intensification of Re, the improvement of lid velocity of the octagonal's upper wall produce a single primary vortex (Fig. 6(a)). Threfore, the force convection becomes stronger due to the increase of lid velocity around the obstacle within the cavity. The fluid follows on the upper wall as it transmitted from left to right direction in accordance with the lid velocity. As the magnitude of Re rises, there is an upsurge the fluid velocity from left to right through the top surface, reaching its optimum level at $Re = 200$. The similar findings have also been observed from Ali et al. study [28]. Conversely, Fig. 6(b) illustrates way isotherm contours regulate fluid temperature by showing how heat transmission within the fluid domain improves by raising the value of Re. There is evidence of spontaneous convection for low values of Re ($Re = 10$). As a result, from the leftward heated cylinder to the rightward cold one, the isotherm lines change equally. The rising magnitude of Re ($Re = 50$) causes the lid velocity to increase, and the upper wall's lid velocity causes mixed convection flow within the cavity domain. The stratification of the isotherm lines have been distributed of the most of the cavity domain with the higher value of Reynolds number that might also been observed Akhter et al. [30,46].

In order to measure the impact of Reynolds number on the velocity distribution along the horizontal representative length of the of the cavity, the non-dimensional characteristic velocity (alongside the Y-axis) over the whole domain has been determined and illustrated in Fig. 7. This magnitude of the velocity profile is calculated along the line (0.5, 0) to (0.5, 1). Due to the enhancement of Re, the fluid velocity is increasing near the boundary of the domain (Fig. 7). There is an 83.25 % rise in the heat exchange rate over the prior value. The overall calculated heat transport rate from the heated surface to cooled surface is measured 36.28 % for increasing Reynolds number ranging from $Re = 50$ to $Re = 100$. and 22.27 % for $Re = 200$.

4.2. Impact of Hartman number

Assuming that $Pr = 6.9$, $Ri = 1$, $Re = 100$ and $\phi = 0.02$, the streamline and isotherm contours in Figs. 8 and 9 illustrate the effects of

Table 5
Result comparision with Islam et al. [10] utilizing Nu_{av} keeping $Ha = 50$, $\phi = 0.05$.

Re	Islam et al. [10]	Our Findings	Error (%)
10	2.3517	2.3492	0.1
105	3.7066	3.6672	1.06
200	4.1984	4.1852	0.31

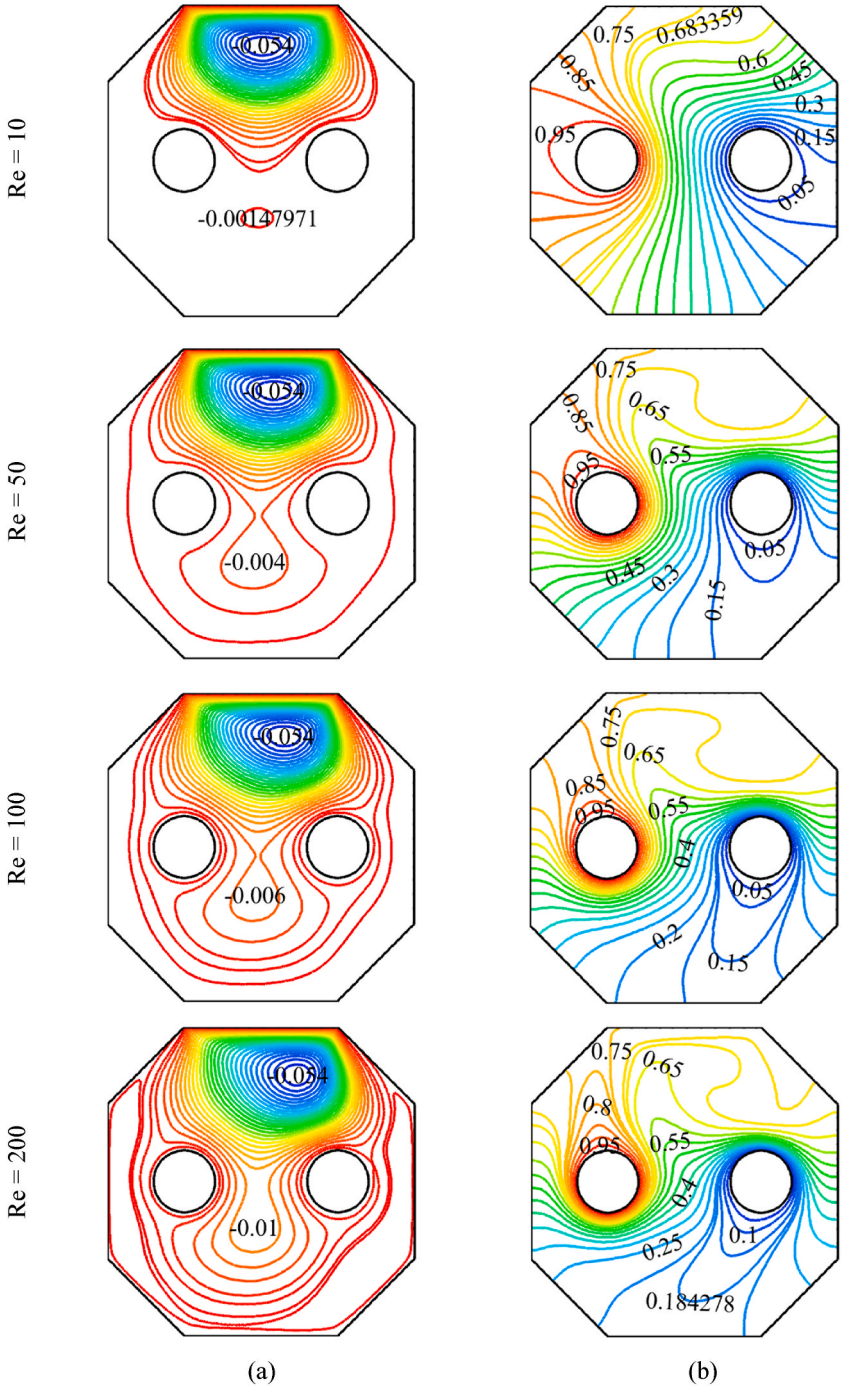

Fig. 6. Impact of Re on: (a) streamlines, and (b) isotherms.

the *Ha* on thermal transit and fluid motion. In reality, *Ha* illustrates that magnetic force is controlled on this octagonal heat exchanger. As shown in Fig. 8(a), the overall thickness of streamlines is highest when the field of magnetic attraction is not occupied, as well as *Ha* = 0. Furthermore, fluid flow is maximized if there is no magnetic force (*Ha* = 0) as opposed to a magnetic field (*Ha* = 25, 50, 100). Consequently, the isotherm contours will have an identical form in the vertical plane when the convection type of heat transmission progressively yields up to the conduction manner. Because of the magnetism effect, a resistance force known as the Lorentz force is present inside the barrier and has the potential to slow down the mobility of the nanofluid itself. Which is the phenomenon's physical explanation. Hence, the streamlines and the upper lid surfaces are very close together. Additionally, as seen in Fig. 9, the fluid velocity is likewise reduced function of *Ha*.

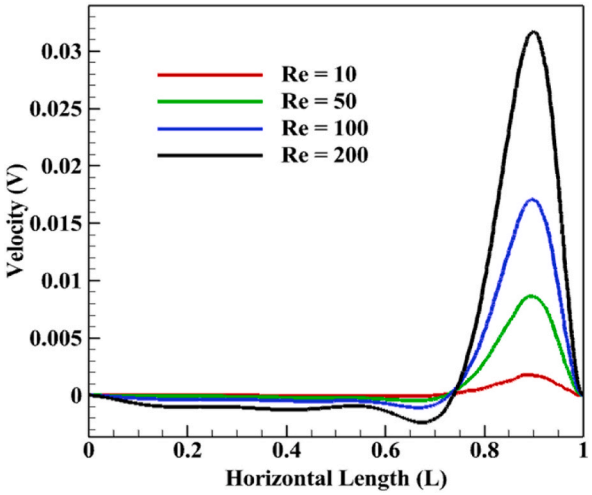

Fig. 7. Impact of Re on fluid velocity.

This velocity profile is calculated along the line (0.5, 0) to (0.5, 1). Additionally, when *Ha* grew, Fig. 8(b) isotherm contours depict a minor shift in the temperature field. The heat transmission rate (Nu_{av}) is at its highest when the magnetic effect is dormant ($Ha = 0$). For $Ha = 25$, the Nu_{av} is lowered by 25.43 %. When the *Ha* number is adjusted from 25 to 50, the falling rate is 29.53 %. Furthermore, at the highest magnetic impact value ($Ha = 100$), this lowered rate is 23.82 %. Similar results have also been noted in the study conducted by Islam et al. [2,47].

4.3. Impact of nanoparticle volume fraction

Figs. 10–11 shows the results of ϕ (for 0, 0.025, 0.05, and 0.1) on the streamlines, isotherms, for an octagonal heat exchanger enclosure when Pr = 6.9, Ri = 1, Re = 100, and $Ha = 10$. Fig. 10(a) shows that the fluid flow pattern is impacted by fluctuations of ϕ. Firstly, observe the base fluid mode (for $\phi = 0$) at the equilibrium of the buoyant forces and inertia forces. Consequently, the top lid walls experience a movement effect from the core vortex. Also, the consistent streamlines clearly show the control of mixed convective fluid movements. Furthermore, the vortex in the streamlines widens as the value of ϕ increases. The physical explanation for these specific streamlining shapes is well known. Because due to add of nanoparticles into water, the friction among nanoparticles and water molecules are occurred. As a result, the flid movement reduce slightly, which is clearly explained in Fig. 11. This velocity profile is calculated along the line (0.5, 0) to (0.5, 1). As the value of ϕ grows, the streamline pattern closely resembles pure conduction.

Additionally, a negligible effect of hybrid nanofluids on convection is found upon the adding of hybrid nanoparticles in base fluid within the cavity. On the other hand, the isotherm lines in Fig. 10(b) and the velocity field show that the rate of thermal transit increases as ϕ values rise where the Nu_{av} is also being increased.

4.4. Effect of hybrid nanofluid

Here, Nu_{av} is utilized with the effects of Re and *Ha* to explain the rate of heat transport for various fluids. The impact of *Ha* on Nu_{av} for various fluid types, with or without nanoparticles present in the base fluid, is depicted in Fig. 12(a). Clearly, Nu_{av} steadily declines as the magnetic effect (*Ha*) proliferation's. The Nu_{av} is raised by 11.23 % and 19.76 %, respectively, for TiO_2-H_2O and Cu-TiO_2 nanofluids. Furthermore, the Nu_{av} is quickly flipped for Cu-TiO_2-H_2O hybrid nanofluid, which is 25.75 % higher than in H_2O. Furthermore, as Ra rises, Nu_{av} grows monotonically for pure fluid (H_2O), TiO_2-H_2O nanofluid, Cu-H_2O nanofluid, and Cu-TiO_2-H_2O hybrid nanofluid, as shown in Fig. 12(b). Additionally, the Nu_{av} increases by 3.46 % for TiO_2-H_2O nanofluid, and 4.93 % for Cu-H_2O nanofluid. Also, the rate of Nu_{av} is swiftly flipped for the Cu-TiO_2-H_2O nanofluid, which is 6.73 % more than H_2O.

4.5. Response surface methodology

The response function's impact from the relevant parameters (*Ha*, Re, and ϕ) Nu_{av} is explained by the statistical RSM method. One of the best methods for modeling multidimensional situations where input elements simultaneously affect the responses that pique attention is response system modeling (RSM) [48,49]. Even though there are numerous RSM models, the second-order RSM model often provides a good enough approximation of the response. According to some, the quadratic RSM model is:

$$y = z_0 + \sum_{i=1}^{3} z_i x_i + \sum_{i=1}^{3} z_{ii} x_i^2 + \sum_{i=1}^{3} z_{ij} x_i x_j \tag{29}$$

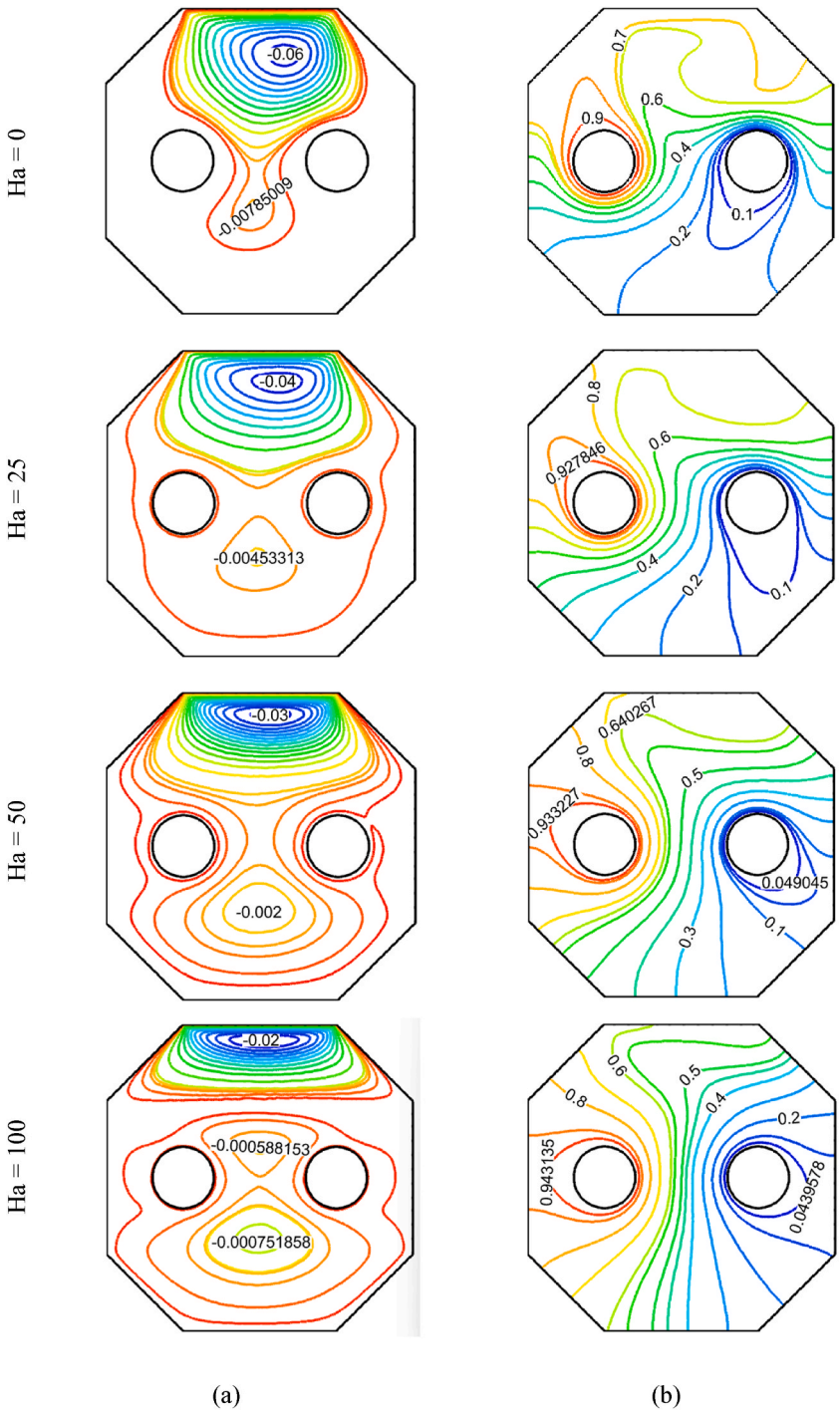

Fig. 8. Impact of Hartman number on: (a) streamlines, and (b) isotherms.

Here, the intercept term is z_0, the response function (output) denoted by y, the linear term of the ith factor regression coefficient is denoted by z_i, the coefficient of quadratic term for ith factor z_{ii}, and the collaboration of ith and jth factors are denoted by z_{ij}. Furthermore, the pertinent parameters *Ha*, ϕ, and Re are used as independent factors, while Nu_{av} is considered as the response faction (y). Finding a best-fitted correlation between y and independent factors is the major goal. Here, a second-order RSM model with a CCD basis is used [50]. The range of the independent parameters Re, *Ha*, and ϕ in this study is and there are 20 runs in this CCD-based RSM model (8 cube, 6 center, and 6 axial points). Table 6 provides information on the codded levels of the parameter for CCD. Table 7 shows the computational run parameters for both coded and actual values centered on the CCD.

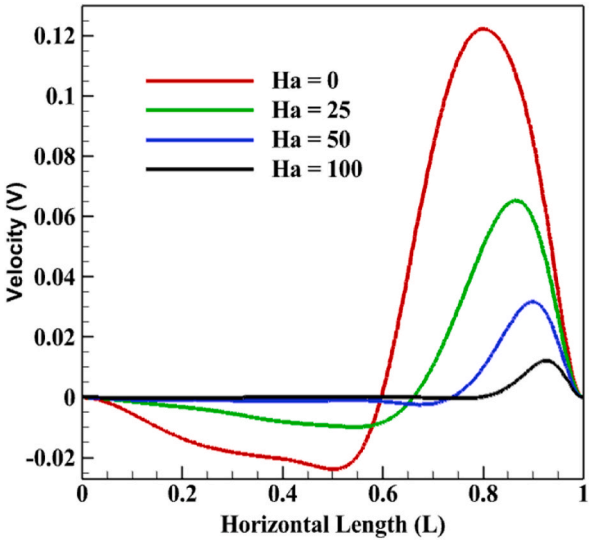

Fig. 9. Impact of *Ha* on fluid velocity.

Table 8 displays the results of the statistical analysis using RSM. The maximum number of independent terms in this model is represented by the degrees of freedom (DOF). One method for representing the overall variance resulting from several factors is the total sum of squares (SS). The Adj. SS, have a significant value of 316.87. The F-value, which is 31.95 and indicates that noise does not affect the results, indicates that the Nu_{av} model is statistically significant. Furthermore, the p-value, which determines the likelihood that the null hypothesis would be true for a specific statistical model, is a highly significant signal of this statistical investigation. A small p-value (typically $\leq$0.05) indicates that the predicted outcome is appropriate. It is evident from Table 8 that all input elements are important for this approach. Furthermore, the model statistical analysis and testing methods indicate high values of the R^2 (96.64 %) for Nu_{av}, indicating that this model is appropriate for calculating the Nu_{av} response function. Although the model modified R^2 (93.6 %) is lower than R^2 (96.64 %), the model nevertheless sufficiently explains the experimental data. Another important metric is Lack of Fit, which requires very little to be a suitable model. The general models that RSM created to examine the connection between the effective input parameters (Re, *Ha*, and ϕ) and the response (Nu_{av}) are as follows:

$$y = z_0 + z_1 Re + z_2\, Ha + z_3\, \varphi + z_{11} Re^2 + z_{22}\, Ha^2 + z_{33}\, \varphi^2 + z_{12} Re.Ha + z_{13} Re.\varphi + z_{23}\, Ha.\varphi\} \quad (30)$$

Here, z_0, z_1, z_2, z_3, z_{11}, z_{22}, z_{33}, z_{12}, z_{13}, and z_{23} are the coefficients of the best fitted regression model for this RSM model. Additionally, Table 9 displays the coded units that are used to compute the projected coefficients of equation (30) for Nu_{av}. To create a suitable regression equation, solely those terms with low p-values ($\leq$0.05) are considered. On the other hand, the terms that are not significant are disregarded (bold indicated). That is, important terms for the response function (Nu_{av}) are Re, *Ha*, ϕ, Re. *Ha*, Re. ϕ, and *Ha*. ϕ. On the other hand, since Re^2, ϕ^2 and Ha^2 have no bearing whatsoever on Nu_{av}, they should not be included in the final best-fitted regression model.

That is, for Nu_{av} regression equation (30) the terms Re^2, Ha^2 and ϕ^2 have no bearing at all. Therefore, the following mathematical summary may be used to represent the association between Nu_{av} and the components Re, *Ha* and ϕ:

$$Nu_{av} = 1.21830 + 0.0439Re - 0.1017Ha + 93.1248\, \varphi - 0.00098Re.Ha + 1.7529Re.\varphi - 1.1886Ha.\, \varphi\} \quad (31)$$

Here, equation (31) is the best fitted correlation between the Nu_{av} and the independent factors.

4.6. Response surface analysis

Figs. 13–15 show 2D and 3D contour plots of the RSM-created response surface (Nu_{av}) to explore the effect of included factors on the response function (Nu_{av}). The influence of Re and *Ha* on Nu_{av} is seen in Fig. 13(a). This 2D contour map makes it evident that, although the other factor ϕ (0.025) is unchanged, the Nu_{av} increases when Re is being raised and *Ha* is being decreased. The Nu_{av} reaches its maximum at Re = 200 and *Ha* = 0, and its minimum at Re = 10 and *Ha* = 100. Moreover, Fig. 13(b) illustrates a 3D surface map that shows both Re and *Ha* affect Nu_{av}. That is, these two response surfaces display the same behavior which is similar to the outcomes of the applied FEM. Similarly, Fig. 14(a) expresses a 2D graphical depictions that show that with intensification of ϕ and decrease of *Ha* causing the response function to rise. At that point, the value of Re stays at 100. When ϕ = 0.1 and *Ha* = 0, the Nu_{av} gets uppermost value, and when ϕ = 0 and *Ha* = 100, it is at its bottommost. Furthermore, the influence of *Ha* and ϕ on the response function is shown in a 3D perspective in Fig. 14(b). Similarly, Fig. 15 illustrates Nu_{av} oscillations with Re and ϕ once again. In Fig. 15

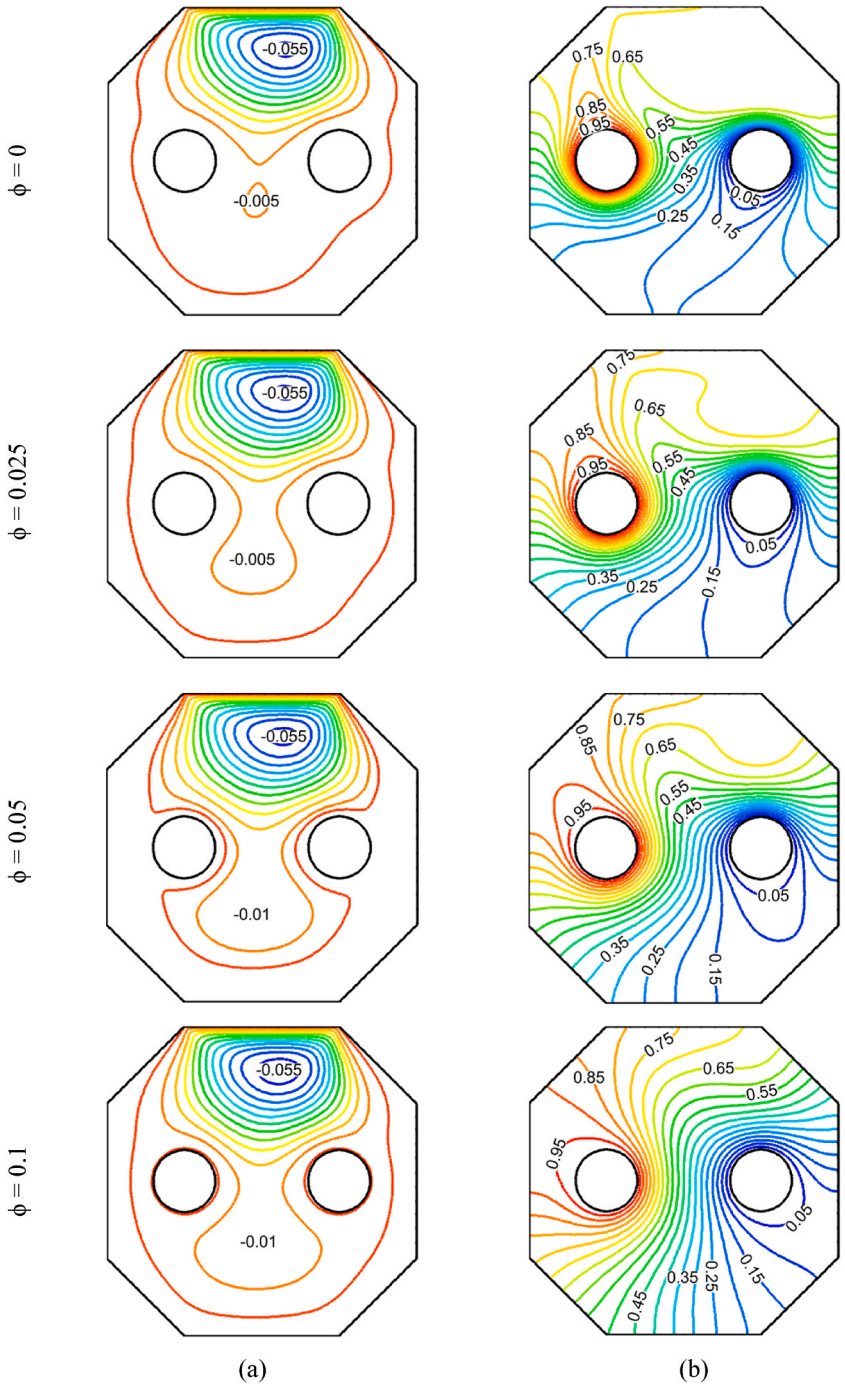

Fig. 10. Impact of ϕ on: (a) streamlines, and (b) isotherms.

(a), the Nu_{av} rises when both the values of Re and ϕ are enhanced while holding another component ($Ha = 10$) constant. The Nu_{av} reaches its maximum at Re = 200 and ϕ = 0.1, and its minimum at Re = 10 and ϕ = 0. Additionally, Fig. 15(b) depicts a different 3D surface plot that shows how Re and ϕ affect Nu_{av} these two response surface plots show a similar action on Nu_{av}.

To prove the validity statistically of the outcomes of the applied FEM, the statistical technique RSM is also used. The outcomes of the FEM are homologous to the RSM. This agreement strongly supports the proposed mixed convective numerical analysis using hybrid nanofluid.

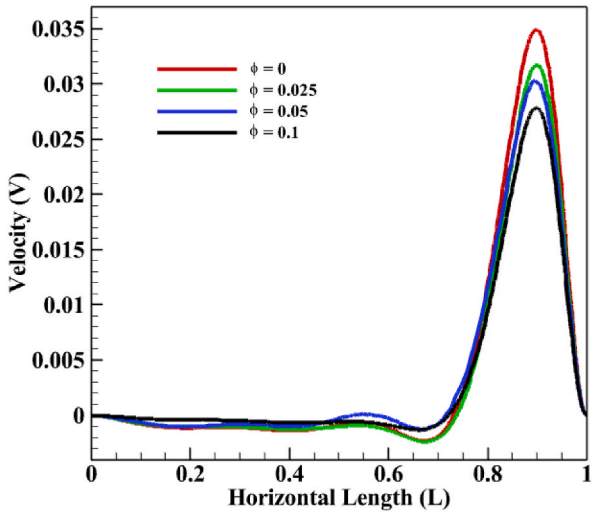

Fig. 11. Impact of ϕ on fluid velocity.

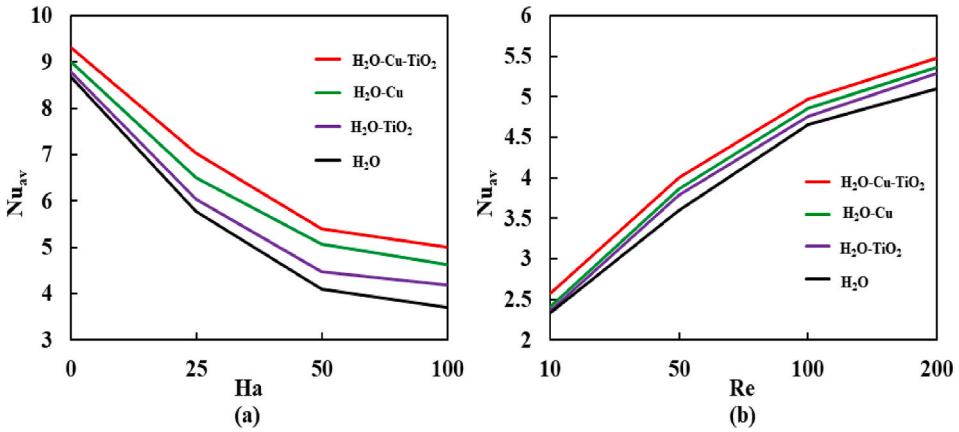

Fig. 12. Importance of addition of ϕ using Nu_{av} for numerous *Ha* and Re value.

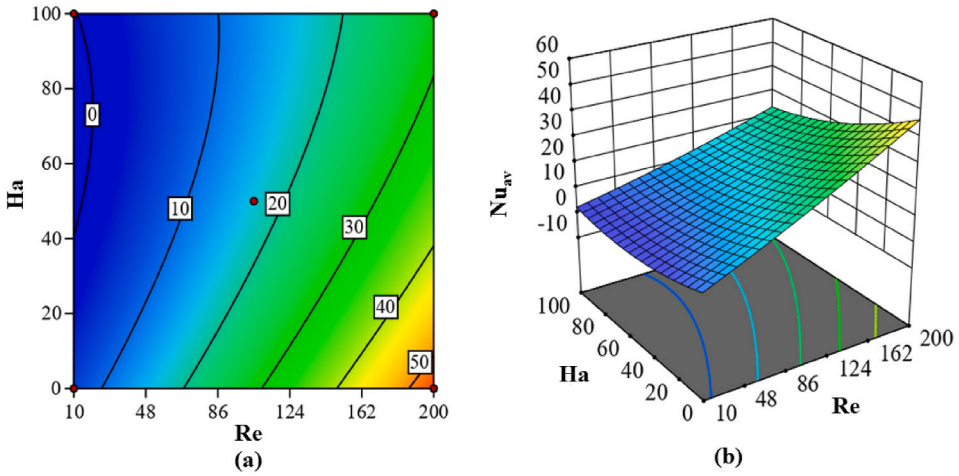

Fig. 13. Effect on Nu_{av} for Re and *Ha*: (a) 2D sight; (b) 3D sight.

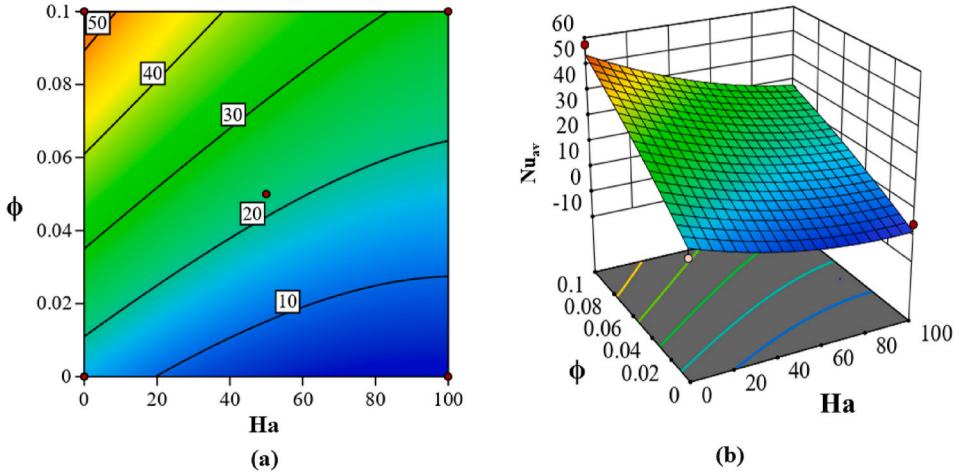

Fig. 14. Effect on Nu_{av} for ah and ϕ: (a) 2D sight; (b) 3D sight.

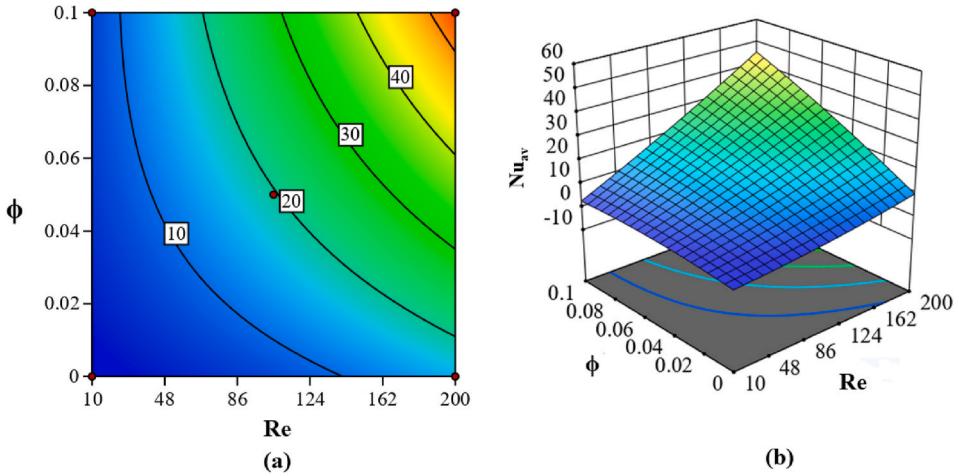

Fig. 15. Effect on Nu_{av} for Re and ϕ: (a) 2D sight; (b) 3D sight.

Table 6
CCD design factors and codded levels.

Factors	Level		
	−1 (lowest)	0 (medium)	1 (highest)
Re	10	105	200
Ha	0	50	100
ϕ	0	0.05	0.1

5. Conclusions

The mixed convection properties of hybrid nanofluid (Cu-TiO_2-H_2O) has been delved in a specially designed octagonal heat exchanger with two heating and cooling source inside cavity domain. The suspended nanofluids in the water-based mixture exhibit the ability to undergo phase transitions, changing between different fluid states as they pass through the enclosing domain. The influence of the most significant parameters Re, *Ha*, and ϕ on Nu_{av} are analysed using the streamline profiles, isotherm line, and velocity field with 2D and 3D investigation. The accumulation of hybrid nanoparticles significantly changes the heat transfer rate as well. The finite element scheme was applied to integrate the heat transfer underlying the governing equations. The results are rigorously displayed using a range of Nusselt number to provide a thorough assessment of heat transfer and detailed contour plots of field variables, which broaden our understanding of the underlying heat transfer phenomenon from a physical standpoint. The main findings of the study are as follows:

Table 7
Levels of input factors and response function.

Run Order	Codded Values			Real Values			Response
	A: Re	B: *Ha*	C: ϕ	Re	*Ha*	ϕ	Nu_{av}
1	0	0	0	200	100	0	4.2407
2	−1	0	0	200	100	0.1	26.157
3	0	−1	0	200	0	0.1	57.397
4	0	0	0	105	100	0.05	9.1101
5	0	1	0	10	0	0	3.3431
6	0	0	0	105	50	0.1	14.282
7	1	1	−1	200	50	0.05	20.855
8	0	0	1	10	100	0	2.6246
9	−1	−1	−1	10	0	0.1	3.8402
10	−1	1	1	105	0	0.05	20.498
11	−1	−1	1	200	0	0	11.654
12	0	0	0	105	50	0.05	10.223
13	1	−1	1	105	50	0.05	10.223
14	0	0	−1	105	50	0.05	10.223
15	−1	1	−1	105	50	0.05	10.223
16	0	0	0	10	50	0.05	3.0253
17	1	−1	−1	105	50	0	4.2483
18	1	0	0	10	100	0.1	3.1759
19	0	0	0	105	50	0.05	10.223
20	1	1	1	105	50	0.05	10.223

Table 8
Analysis of variance for Nu_{av}.

Source	DOF	Adj. SS	F-Value	p-Value	Comment
Model	9	316.87	31.95	<0.0001	**Significant**
Re	1	1087.74	109.67	<0.0001	
Ha	1	264.44	26.66	<0.0004	
ϕ	1	620.02	62.51	<0.0001	
Re^2	1	3.75	0.3784	**0.5522**	
Ha^2	1	44.71	4.51	**0.0597**	
ϕ^2	1	6.24	0.6294	**0.4460**	
Re*Ha	1	173.64	17.51	0.0019	
Re*ϕ	1	554.63	55.92	<0.0001	
*Ha*ϕ	1	70.64	7.12	0.0235	
Lack-of-Fit	5	19.84	–	–	**Insignificant**
Pure Error	5	0.000	–	–	
Total	19	2951.01	–	–	

**Here, $\mathbf{R^2 = 96.64\ \%}$, **Adjusted $\mathbf{R^2 = 93.61\ \%}$.

Table 9
Regression coefficients for Nu_{av} that are predicted based on RSM.

Coefficients	z_0	z_1	z_2	z_3	z_{11}	z_{22}	z_{33}	z_{12}	z_{13}	z_{23}
Values	1.2183	0.0439	−0.1017	93.1248	0.00012	0.00161	−602.672	−0.00098	1.7529	−1.1886
p-values	–	<0.0001	0.0004	<0.0001	**0.5522**	**0.0597**	**0.4460**	0.0019	<0.0001	0.0235

1. The mixed convective heat exchanger processes are enhanced by the expansion of Re, whereas the substantial effect of the magnetic field reduces total energy exchange and thermal transport mechanisms.
2. The increasing values of Re from 10 to 50, 100, and 200 have resulted in rising the rate of Nu_{av} by 83.25 %, 36.28 %, and 22.27 %, respectively.
3. The mean Nusselt number, Nu_{av} is negatively impacted by the magnetic field. The decreasing rates of the Nu_{av} are 25.43 %, 29.53 %, and 23.82 %, respectively, with rising the value of *Ha* from 0 to 25, 50, and 100.
4. The 2D and 3D response surfaces obtained from RSM are geometrically explained by using RSM where the findings are almost homologous to the results of FEM.
5. The size of the nanoparticles of hybrid nanofluid (Cu-TiO_2-H_2O) can be employed up to 10 % (0.1) and Re = 200 keeping *Ha* = 0 in order to create an efficient mixed convective octagonal heat exchanger.

Data availability

The study uses a numerical method, and the findings do not include any data.

Funding

This research received no external funding.

CRediT authorship contribution statement

Md. Yousuf Ali: Writing – review & editing, Writing – original draft, Validation, Software, Methodology, Formal analysis, Conceptualization. **Saiful Islam:** Writing – review & editing, Software, Formal analysis, Conceptualization. **M.A. Alim:** Writing – review & editing, Supervision, Methodology, Formal analysis. **Rejowan Ahmed Biplob:** Writing – review & editing, Software, Conceptualization. **Md. Zohurul Islam:** Writing – review & editing, Validation, Software, Formal analysis, Investigation.

Declaration of competing interest

The authors declare that they have no known competing financial interests or personal relationships that could have appeared to influence the work reported in this paper.

Acknowledgement

The authors would like to thank the Ministry of Science and Technology (MoST) of Bangladesh for its financial support. Also, convey sincere appreciation to the Department of Mathematics at Bangladesh University of Engineering and Technology (BUET) for technical assistance.

Nomenclature

c_p	Specific heat at constant pressure ($J.kg^{-1}\ K^{-1}$)
k	Thermal conductivity ($W.m^{-1}\ K^{-1}$)
g	Gravitational acceleration ($m.s^{-1}$)
Ri	Richardson Number
Nu	Nusselt number
Ha	Hartmann Number
Pr	Prandtl number
P	Pressure without dimension
U, V	Velocity component without dimension
X, Y	Dimensionless Cartesian coordinates
u, v	Dimensional velocity component ($m.s^{-1}$)
x, y	Dimensional Cartesian coordinates
TiO_2	Titanium Oxide
Cu	Copper
L	Enclosure length (m)

Greek symbols

α	Thermal diffusivity ($m^2\ s^{-2}$)
β	Coefficient of thermal expansion (K^{-1})
ϕ	Particle concentration
θ	Non-dimensional temperature
μ	Dynamic viscosity ($kg.m^{-1}\ s^{-1}$)
ν	Kinematic viscosity ($m^2\ s^{-1}$)
ρ	Density ($kg.m^{-3}$)
Ω	Vorticity vector
σ	Electric conductivity ($\Omega^{-1}.\ m^{-1}$)
ψ	Stream function

Subscripts

hnf	Hybrid nanofluid
bf	Base fluid
av	Average
T_c	Cold surface

T_h	Heated surface
sp	Solid particle
HS	Heated surface

References

[1] M. Sheikholeslami, Z. Said, M. Jafaryar, Hydrothermal analysis for a parabolic solar unit with wavy absorber pipe and nanofluid, Renew. Energy 188 (2022) 922–932.
[2] S. Islam, T. Bairagi, T. Islam, B.M.J. Rana, S.K. Reza-E-Rabbi, M.M. Rahman, Heatline visualization in hydromagnetic natural convection flow inside a prismatic heat exchanger using nanofluid, International Journal of Thermofluids 16 (2022) 100248.
[3] A. Ahmadi, M.A. Ehyaei, A. Doustgani, M.E.H. Assad, F. Esmaeilion, A. Hmida, A. Razmjoo, Recent progress in thermal and optical enhancement of low temperature solar collector, Energy Systems 14 (1) (2023) 1–40.
[4] P. Venkataramana, P.V. Kumar, B.B. Krishna, Thermal and flow performance in a CLPHP with Al2O3/copper nanofluids: application in microelectronics and power generation, Mater. Today: Proc. (2023).
[5] J.C. Maxwell, Treatise on Electricity and Magnetism, Clarendon Press, Oxford, 1873.
[6] S.U. Choi, J.A. Eastman, *Enhancing Thermal Conductivity of Fluids with Nanoparticles* (No. ANL/MSD/CP-84938; CONF-951135-29), Argonne National Lab. (ANL), Argonne, IL (United States), 1995.
[7] M. Zarringhalam, A. Karimipour, D. Toghraie, Experimental study of the effect of solid volume fraction and Reynolds number on heat transfer coefficient and pressure drop of CuO–water nanofluid, Exp. Therm. Fluid Sci. 76 (2016) 342–351.
[8] M.G. Ibrahim, Numerical simulation to the activation energy study on blood flow of seminal nanofluid with mixed convection effects, Comput. Methods Biomech. Biomed. Eng. 26 (3) (2023) 315–325.
[9] A. Hossain, M.M. Molla, M. Kamrujjaman, M. Mohebujjaman, S.C. Saha, MHD mixed convection of non-Newtonian bingham nanofluid in a wavy enclosure with temperature-dependent thermophysical properties: a sensitivity analysis by response surface methodology, Energies 16 (11) (2023) 4408.
[10] S. Islam, M.M. Islam, B.M.J. Rana, M.S. Islam, S. Reza-E-Rabbi, M.S. Hossain, M.M. Rahman, Numerical investigation with sensitivity study of MHD mixed convective hexagonal heat exchanger using TiO2–H2O nanofluid, Results in Engineering 18 (2023) 101136.
[11] H.F. Oztop, A.Z. Sahin, H. Coşanay, I.H. Sahin, Three-dimensional computational analysis of performance improvement in a novel designed solar photovoltaic/thermal system by using hybrid nanofluids, Renew. Energy 210 (2023) 832–841.
[12] A.A. Minea, W.M. El-Maghlany, Influence of hybrid nanofluids on the performance of parabolic trough collectors in solar thermal systems: recent findings and numerical comparison, Renew. Energy 120 (2018) 350–364.
[13] S. Kumar, B.R. Kumar, S.V.S.S.N.V.G. Krishna Murthy, D. Parmar, Double-diffusive convective flow of hybrid nanofluid in an inverted T-shaped porous enclosure: a numerical study, Numer. Heat Tran., Part A: Applications (2023) 1–25.
[14] V. Dubey, A.K. Sharma, A short review on hybrid nanofluids in machining processes, Advances in Materials and Processing Technologies 9 (1) (2023) 138–151.
[15] Z. Abdel-Nour, A. Aissa, F. Mebarek-Oudina, A.M. Rashad, H.M. Ali, M. Sahnoun, M. El Ganaoui, Magnetohydrodynamic natural convection of hybrid nanofluid in a porous enclosure: numerical analysis of the entropy generation, J. Therm. Anal. Calorim. 141 (2020) 1981–1992.
[16] K.V. Modi, P.R. Patel, S.K. Patel, Applicability of mono-nanofluid and hybrid-nanofluid as a technique to improve the performance of solar still: a critical review, J. Clean. Prod. (2023) 135875.
[17] L.S. Sundar, Synthesis and characterization of hybrid nanofluids and their usage in different heat exchangers for an improved heat transfer rates: a critical review, Engineering Science and Technology, an International Journal 44 (2023) 101468.
[18] X. Wang, Q. Wen, J. Yang, S. Shittu, X. Wang, X. Zhao, Z. Wang, Heat transfer and flow characteristic of a flat confined loop thermosyphon with ternary hybrid nanofluids for electronic devices cooling, Appl. Therm. Eng. 221 (2023) 119758.
[19] K.V. Nagaraja, U. Khan, J.K. Madhukesh, A.M. Hassan, B.C. Prasannakumara, N. Ben Kahla, J. Singh Chohan, Heat and mass transfer analysis of assisting and opposing radiative flow conveying ternary hybrid nanofluid over an exponentially stretching surface, Sci. Rep. 13 (1) (2023) 14795.
[20] H. Tao, M.S. Aldlemy, O.A. Alawi, H.M. Kamar, R.Z. Homod, H.A. Mohammed, Z.M. Yaseen, Energy and cost management of different mixing ratios and morphologies on mono and hybrid nanofluids in collector technologies, Engineering Applications of Computational Fluid Mechanics 17 (1) (2023) 2164620.
[21] M.Y. Ali, M.A. Alim, M.M. Karim, Mixed convective heat transfer analysis by heatlines on a lid-driven cavity having heated wavy wall containing tilted square obstacle, Math. Probl Eng. 2023 (2023).
[22] S.E. Ahmed, Z. Raizah, A.A. Arafa, S.A. Hussein, FEM treatments for MHD highly mixed convection flow within partially heated double-lid driven odd-shaped enclosures using ternary composition nanofluids, Int. Commun. Heat Mass Tran. 145 (2023) 106854.
[23] K. Chowdhury, M.A. Alim, Mixed convection in a double lid-driven wavy shaped cavity filled with nanofluid subject to magnetic field and internal heat source, J. Appl. Math. 2023 (2023).
[24] S. Yeasmin, M.M. Billah, M.Z. Molla, K.E. Hoque, Numerical analysis of unsteady mixed convection heat transfer characteristics of nanofluids confined within a porous lid-driven L-shaped cavity, International Journal of Thermofluids 16 (2022) 100218.
[25] M.D. Garmroodi, A. Ahmadpour, F. Talati, MHD mixed convection of nanofluids in the presence of multiple rotating cylinders in different configurations: a two-phase numerical study, Int. J. Mech. Sci. 150 (2019) 247–264.
[26] M.S. Ishak, A.I. Alsabery, I. Hashim, A.J. Chamkha, Entropy production and mixed convection within trapezoidal cavity having nanofluids and localised solid cylinder, Sci. Rep. 11 (1) (2021) 14700.
[27] M.M. Ali, R. Akhter, M.A. Alim, Performance of flow and heat transfer analysis of mixed convection in Casson fluid filled lid driven cavity including solid obstacle with magnetic impact, SN Appl. Sci. 3 (2021) 1–15.
[28] M.M. Ali, R. Akhter, M.A. Alim, Magneto-mixed convection in a lid driven partially heated cavity equipped with nanofluid and rotating flat plate, Alex. Eng. J. 61 (1) (2022) 257–278.
[29] S. Hussain, S.E. Ahmed, T. Akbar, Entropy generation analysis in MHD mixed convection of hybrid nanofluid in an open cavity with a horizontal channel containing an adiabatic obstacle, Int. J. Heat Mass Tran. 114 (2017) 1054–1066.
[30] R. Akhter, M.M. Ali, M.M. Billah, M.N. Uddin, Hybrid-nanofluid mixed convection in square cavity subjected to oriented magnetic field and multiple rotating rough cylinders, Results in Engineering 18 (2023) 101100.
[31] D.K. Mandal, N. Biswas, N.K. Manna, R.S.R. Gorla, A.J. Chamkha, Magneto-hydrothermal performance of hybrid nanofluid flow through a non-Darcian porous complex wavy enclosure, Eur. Phys. J. Spec. Top. 231 (13–14) (2022) 2695–2712.
[32] T. Saha, T. Islam, S. Yeasmin, N. Parveen, Thermal influence of heated fin on MHD natural convection flow of nanofluids inside a wavy square cavity, International Journal of Thermofluids 18 (2023) 100338.
[33] I. Zeghbid, R. Bessaïh, Mixed convection and entropy generation in a square cavity using nanofluids, Thermophys. Aeromechanics 25 (2) (2018) 245–256.
[34] A. Maneengam, T. Bouzennada, A. Abderrahmane, K. Guedri, W. Weera, O. Younis, B. Bouallegue, Numerical study of lid-driven hybrid nanofluid flow in a corrugated porous cavity in the presence of magnetic field, Nanomaterials 12 (14) (2022) 2390.
[35] N. Alipour, B. Jafari, K. Hosseinzadeh, Optimization of wavy trapezoidal porous cavity containing mixture hybrid nanofluid (water/ethylene glycol Go–Al2O3) by response surface method, Sci. Rep. 13 (1) (2023) 1635.
[36] O.C. Zienkiewicz, R.L. Taylor, J.Z. Zhu, The Finite Element Method: its Basis and Fundamentals, Elsevier, 2005.

[37] J.H. Saboj, P. Nag, G. Saha, S.C. Saha, Entropy production analysis in an octagonal cavity with an inner cold cylinder: a thermodynamic aspect, Energies 16 (14) (2023) 5487.
[38] T. Saha, G. Saha, N. Parveen, T. Islam, Unsteady magneto-hydrodynamic behavior of TiO2-kerosene nanofluid flow in wavy octagonal cavity, International Journal of Thermofluids 21 (2024) 100530.
[39] R.D. Plant, M.Z. Saghir, Numerical and experimental investigation of high concentration aqueous alumina nanofluids in a two and three channel heat exchanger, International Journal of Thermofluids 9 (2021) 100055.
[40] P. Kapustenko, J.J. Klemeš, O. Arsenyeva, Plate heat exchangers fouling mitigation effects in heating of water solutions: a review, Renew. Sustain. Energy Rev. 179 (2023) 113283.
[41] W. Ajeeb, R.R.T. da Silva, S.S. Murshed, Experimental investigation of heat transfer performance of Al2O3 nanofluids in a compact plate heat exchanger, Appl. Therm. Eng. 218 (2023) 119321.
[42] M.Y. Ali, Print Numerical Investigation of Heatlines on Mixed Convection inside Lid-Driven Cavity Having Heated Wavy Wall with Tilted Square Obstacle, 2022.
[43] R. Hossain, A.K. Azad, M.J. Hasan, M.M. Rahman, Radiation effect on unsteady MHD mixed convection of kerosene oil-based CNT nanofluid using finite element analysis, Alex. Eng. J. 61 (11) (2022) 8525–8543.
[44] M.S. Arif, K. Abodayeh, Y. Nawaz, The modified finite element method for heat and mass transfer of unsteady reacting flow with mixed convection, Frontiers in Physics 10 (2022) 952787.
[45] T. Islam, M.N. Alam, M.I. Asjad, N. Parveen, Y.M. Chu, Heatline visualization of MHD natural convection heat transfer of nanofluid in a prismatic enclosure, Sci. Rep. 11 (1) (2021) 10972.
[46] K. Khanafer, S.M. Aithal, Laminar mixed convection flow and heat transfer characteristics in a lid driven cavity with a circular cylinder, Int. J. Heat Mass Tran. 66 (2013) 200–209.
[47] S. Jakeer, P.B. Reddy, A.M. Rashad, H.A. Nabwey, Impact of heated obstacle position on magneto-hybrid nanofluid flow in a lid-driven porous cavity with Cattaneo-Christov heat flux pattern, Alex. Eng. J. 60 (1) (2021) 821–835.
[48] M.S. Islam, S. Islam, M.N.A.A. Siddiki, Numerical simulation with sensitivity analysis of MHD natural convection using Cu-TiO2-H2O hybrid nanofluids, International Journal of Thermofluids 20 (2023) 100509.
[49] D.C. Montgomery, Design and Analysis of Experiments, John Wiley & sons, 2017.
[50] G.E. Box, K.B. Wilson, On the experimental attainment of optimum conditions, in: Breakthroughs in Statistics: Methodology and Distribution, Springer New York, New York, NY, 1992, pp. 270–310.